

## Hazard assessment of the Tidal Inlet landslide and potential subsequent tsunami, Glacier Bay National Park, Alaska

**Abstract** An unstable rock slump, estimated at  $5$  to  $10 \times 10^6$  m<sup>3</sup>, lies perched above the northern shore of Tidal Inlet in Glacier Bay National Park, Alaska. This landslide mass has the potential to rapidly move into Tidal Inlet and generate large, long-period-impulse tsunami waves. Field and photographic examination revealed that the landslide moved between 1892 and 1919 after the retreat of the Little Ice Age glaciers from Tidal Inlet in 1890. Global positioning system measurements over a 2-year period show that the perched mass is presently moving at 3–4 cm annually indicating the landslide remains unstable. Numerical simulations of landslide-generated waves suggest that in the western arm of Glacier Bay, wave amplitudes would be greatest near the mouth of Tidal Inlet and slightly decrease with water depth according to Green's law. As a function of time, wave amplitude would be greatest within approximately 40 min of the landslide entering water, with significant wave activity continuing for potentially several hours.

**Keywords** Tidal Inlet · Glacier Bay National Park · Rock slump · Glaciation · Rotational landslide · Tsunami · Seismicity · GPS data

### Introduction

Landslides that rapidly enter bodies of water can generate large waves, known as tsunamis. Such waves have caused significant damage worldwide (e.g., Müller 1964, 1968; Slingerland and Voight 1979; Semenza and Ghirotti 2000).

Southeastern Alaska is particularly susceptible to landslide-induced waves because of steep topography, many fjords, high seismicity, and recent glacial retreat removing slope support. Glacier Bay National Park in southeast Alaska (Fig. 1) is within a region of high seismicity, which has had four large magnitude ( $M > 7.0$ ) earthquakes during the twentieth century (Brew et al. 1995). The best known incidences of landslide-generated tsunamis in the region have occurred within Lituya Bay (Fig. 1). There were also submarine landslide-generated tsunamis in many locations during the 1964 earthquake.

From dendrochronologic analysis of trees and observations of trimlines along the slopes of Lituya Bay, at least three landslide-generated waves occurred in 1853–1854, 1874, and October 1936 (Miller 1954). Subsequently, on June 9, 1958, a  $M$  7.9 earthquake on the nearby Fairweather fault (Fig. 1) triggered a rock avalanche of 30 million m<sup>3</sup> that induced a large tsunami through Lituya Bay (Miller 1960). The avalanche generated a wave that ran up 524 m on the opposite close shore and sent a 30-m-high wave beyond Lituya Bay into the Pacific Ocean sinking two of three fishing boats and killing two persons (Miller 1960). Tsunamis generated in Lituya Bay have been analyzed by Fritz et al. (2001) and Mader and Gittings (2002).

A large landslide above the northern shore of Tidal Inlet, in Glacier Bay National Park (Figs. 2, 3, and 4), was recognized in 1964 (Brew et al. 1995). This landslide can potentially generate a tsunami

extending to the West Arm of Glacier Bay. In this paper, we describe the landslide mass, discuss monitoring of the landslide movement using global positioning system (GPS) measurements, and examine models to determine the height, speed, and duration of the potential subsequent landslide-generated tsunami.

### Geographic, geologic, and glacial settings

Glacier Bay National Park is a land of deep fjords, coastal beaches, and glacier-clad, snow-capped mountain ranges that rise to more than 4,500 m. A wet and cool climate supports thick vegetation through much of lower Glacier Bay vacated by retreating glaciers. Glacier Bay was almost completely covered by glacial ice to the outlet into Icy Strait during the Little Ice Age (LIA) between the thirteenth and nineteenth centuries (Goodwin 1988; Larsen et al. 2005; Fig. 1).

Tidal Inlet is located off the West Arm of Glacier Bay (Fig. 1). The northern shore of Tidal Inlet (Fig. 5) consists of two main geologic units—the Pyramid Peak Limestone (DSp; Devonian, 354–417 million of years ago or Silurian, 417–443 millions of years ago) and the Tidal Formation (Stg; Late Silurian) calcareous graywacke and thin-bedded argillite, covered in places by surficial deposits (Qs) (Holocene and/or Pleistocene; Rossman 1963; Brew, written communication, 2002). The DSP comprising the slopes above the landslide is composed of 2-cm- to 1-m-thick beds, light gray to very dark gray (Brew, written communication, 2002). The Stg is exposed near the shoreline on the slopes below the landslide and higher on the slope in the main scarp and consists of thinly bedded argillite, calcareous graywacke, and minor limestone; individual beds are up to several centimeters thick, generally brown to brownish gray. These rocks contain dipping sedimentary structures that are believed to belong to turbidite–fan complexes. The Qs within the region of the recently active landslide are both weathered and heavily fractured. The contact between the DSP and Stg is an unconformity that is obscured in many places by glacial till and by talus covering the middle and lower parts of the hillside resulting from landslide movement (Fig. 5).

Cool temperatures, ample precipitation, and complex high topographic relief of Glacier Bay National Park have resulted in extensive ice fields. Massive Cordilleran ice sheets cyclically expanded and swept seaward across this terrain throughout the Pleistocene. The last glacier maximum came to a close in this region between 10,000 and 12,000 years ago (Miller 1975; Mann 1986; Goodwin 1988) and was followed by the nonglacial Hypsithermal Interval of the Holocene, which lasted from about 8,000 to 4,000 year B.P. The region then experienced several cycles of glacier expansion and contraction during the late Holocene, beginning about 3,000 years ago (Goodwin 1988; Motyka and Beget 1996). The most recent advance, the LIA, spanned a period lasting from the mid-thirteenth century to the late nineteenth century in this region. The LIA expansion filled both arms of Glacier Bay with

**Fig. 1** Location map of Glacier Bay National Park, Alaska, with Tidal Inlet and Blue Mouse Cove along the western arm of Glacier Bay and Lituya Bay along the Pacific coast. Active faults systems of Fairweather–Queen Charlotte Islands and Transition (from Brew et al. 1995). Extent of glacier during Little Ice Age (*dashed line*) and approximate dates and locations of glacial retreat in 1794 near Icy Strait and in 1880 in the northern part of the western arm of Glacier Bay

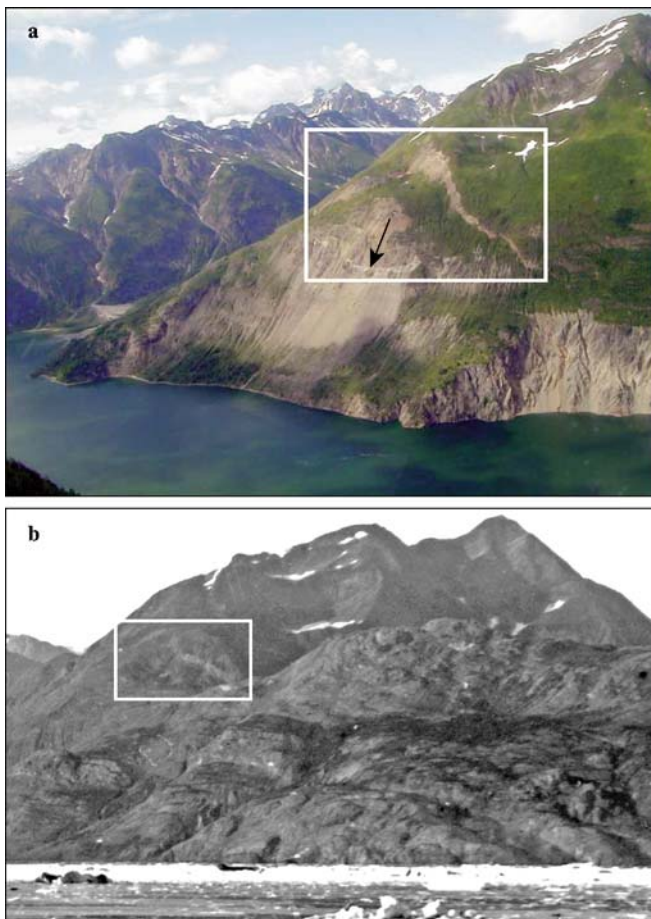
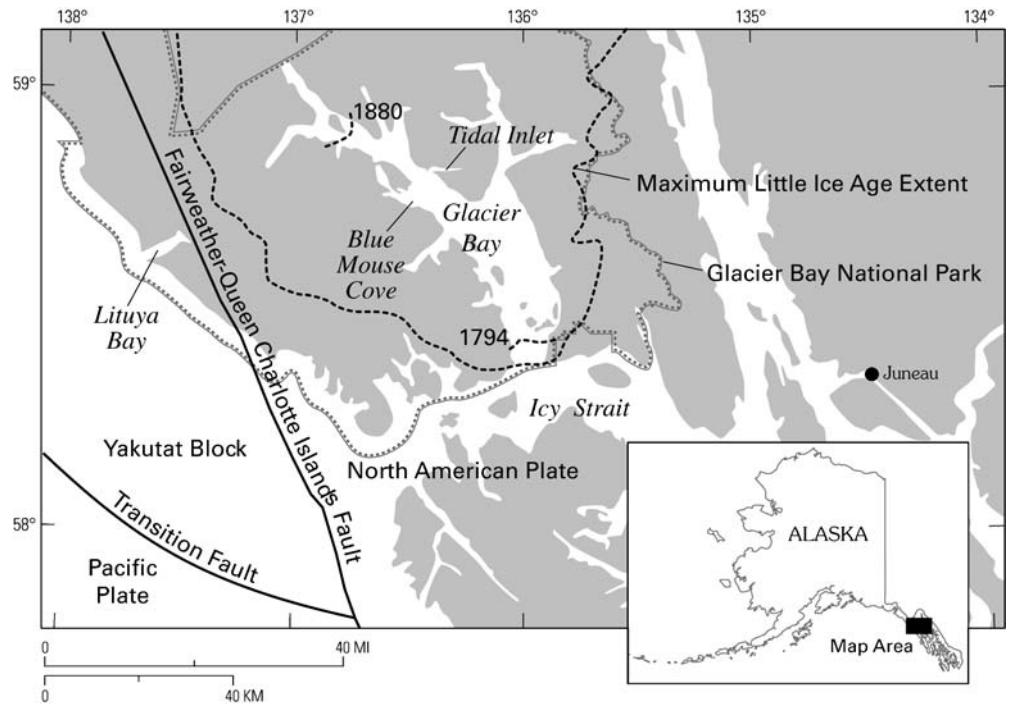


**Fig. 2** Landslide perched above the northern shore of Tidal Inlet with white box outlining upper portion of landslide in both photos. **a** Peak at top right edge of photo is about 1,130 m high. In the lower left, the distance across Tidal Inlet is about 800 m. The arrow shows a white layer of possible limestone. Photograph taken on July 12, 2002. **b** Photo taken by Reid in 1892 showing incipient headwall scarp. Enlarged from a portion of HFReid-346

more than 1-km-thick ice and extended into Icy Strait (Goodwin 1988; Molenaar 1990; Larsen et al. 2005; Fig. 1). Although the LIA continued well into the nineteenth century in many parts of Alaska, a region-wide glacier retreat in southeast Alaska began during the middle to late eighteenth century (Goodwin 1988; Post and Motyka 1995; Motyka and Beget 1996). Nontidewater glaciers retreated very slowly through the late eighteenth and nineteenth centuries, and a few even experienced standstills and slight readvances (Motyka and Beget 1996; Motyka et al. 2002). In contrast, tidewater glaciers in Glacier Bay rapidly retreated by calving during the same period (Goodwin 1988). The main trunk glaciers in Glacier Bay retreated about 120 km from Icy Strait to the head of the west arm of the bay in 180 years (Fig. 1), ranking as the fastest and most prolonged historic tidewater calving retreat in Alaska (Larsen et al. 2005). This retreat caused rapid glacial unloading, causing robust isostatic regional rebound with peak uplift rates of 3.0 cm/year (Larsen et al. 2005).

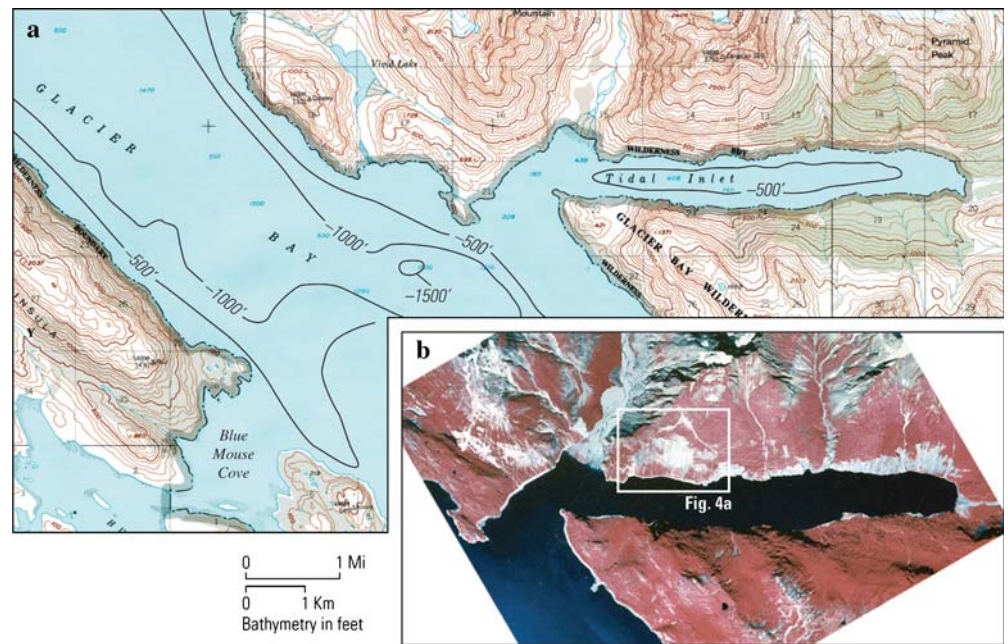
Deglaciation of Tidal Inlet probably proceeded simultaneously with the calving retreat that rapidly depleted ice in both arms of Glacier Bay during the nineteenth century. Maps by Reid (1896) show that Tidal Inlet was devoid of ice by A.D. 1890 except for a small remnant glacier to the east at its headwaters. The retreat of glacial ice decreased lateral support for the hillside.

Post-LIA till deposits several meters in thickness mantle the slopes of the northern shore of Tidal Inlet in many places up to elevations of 600 m. These deposits have been deeply eroded by incised gullies forming steep linear ridges and deeply incised furrows. Within the landslide mass, several rotational movements have formed many steep back-facing scarps, which have displaced the till (Fig. 6). Otherwise, the till shows little sign of surficial erosion.

#### Tidal Inlet landslide

Examination of early historic photos taken by Reid (US Geological Survey [USGS]) in 1892 of the Tidal Inlet area detected an incipient headwall scarp in the location of the present landslide (Fig. 2b). A subsequent photo by Mertie on July 28, 1919 shows that the slide had moved at least 25 m at the top of the northeastern scarp by

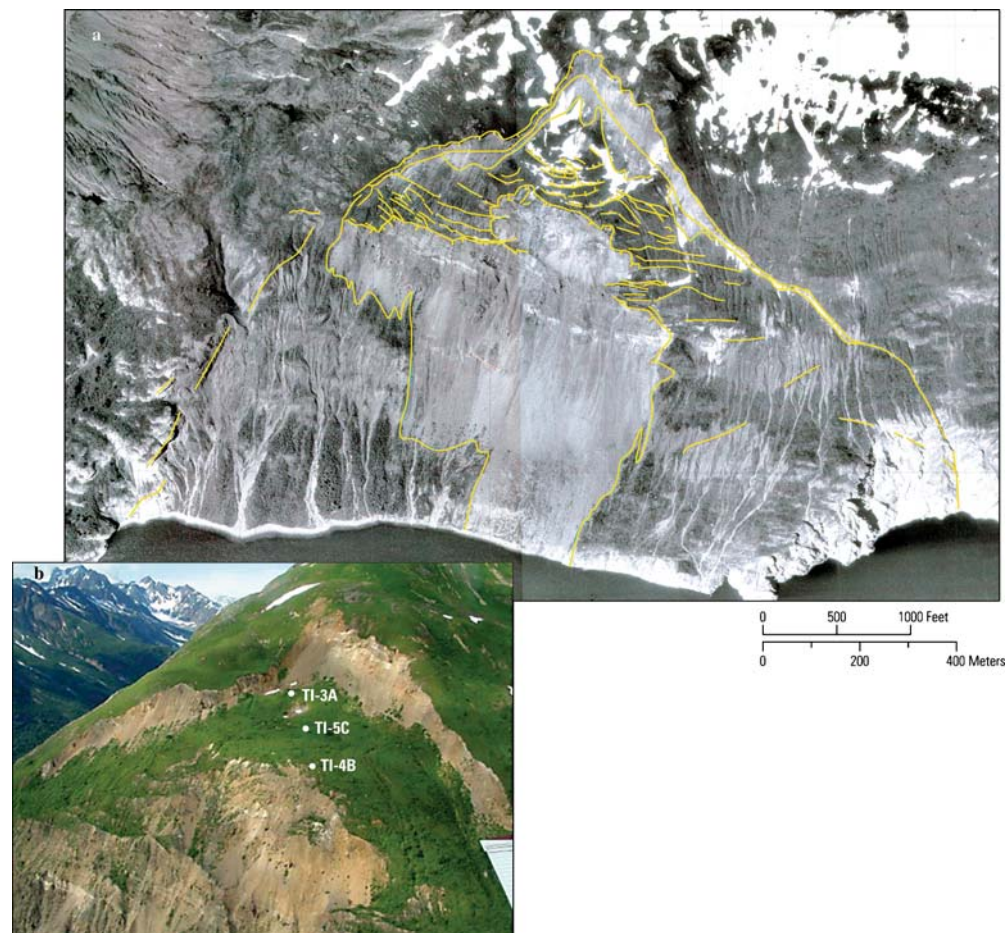
**Fig. 3 a** Topographic map of Tidal Inlet with contour interval of 100 ft. General landslide region within *white box* in both figures. Simplified bathymetry from Hooge et al. (2000). **b** Portion of aerial photograph showing Tidal Inlet landslide impact region into Tidal Inlet shown within the *white square*



1919. Therefore, major movement occurred between 1892 and 1919 after the retreat of the LIA glaciers from Tidal Inlet by A.D. 1890. The timing of landslide movement and the glacial history suggest that glacial debuttressing weakened the slope. Furthermore, the landslide could have been triggered by large earthquakes on September 4 and 10, 1899 ( $M_s=8.5, 8.4$ ) and/or on October 9, 1900

( $M_s=8.1$ ) along the Fairweather–Queen Charlotte Islands fault near Yakutat Block (Fig. 1), about 200 km northwest of Tidal Inlet (Plafker and Thatcher 1982). Although no epicenters of historic large earthquakes have been recorded near Tidal Inlet (Brew et al. 1995), the proximity of Tidal Inlet to major fault systems makes it highly susceptible to strong shaking.

**Fig. 4 a** Observed surface lateral and vertical fractures of entire Tidal Inlet landslide. **b** Recently moving upper portion of Tidal Inlet landslide. Evidence of the secondary recent landslide movement is the lighter bare slope in the center of the photograph. TI-3A, TI-4B, and TI-5C are GPS monitoring points. Photograph taken July 12, 2002



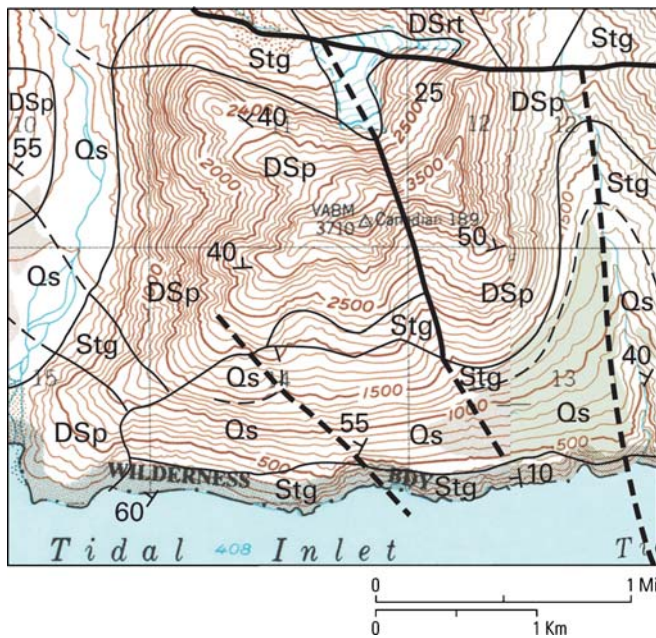


**Fig. 5** Geologic map of the northern portion of Tidal Inlet (modified from Brew, written communication, 2002). Geologic units: *Qs* (surficial deposits), *DSrt* (Undivided Rendu and Tidal Formation Rocks), *DSp* (Pyramid Peak Limestone), and *Stg* (Tidal Formation). Topographic contours are with interval of 100 ft

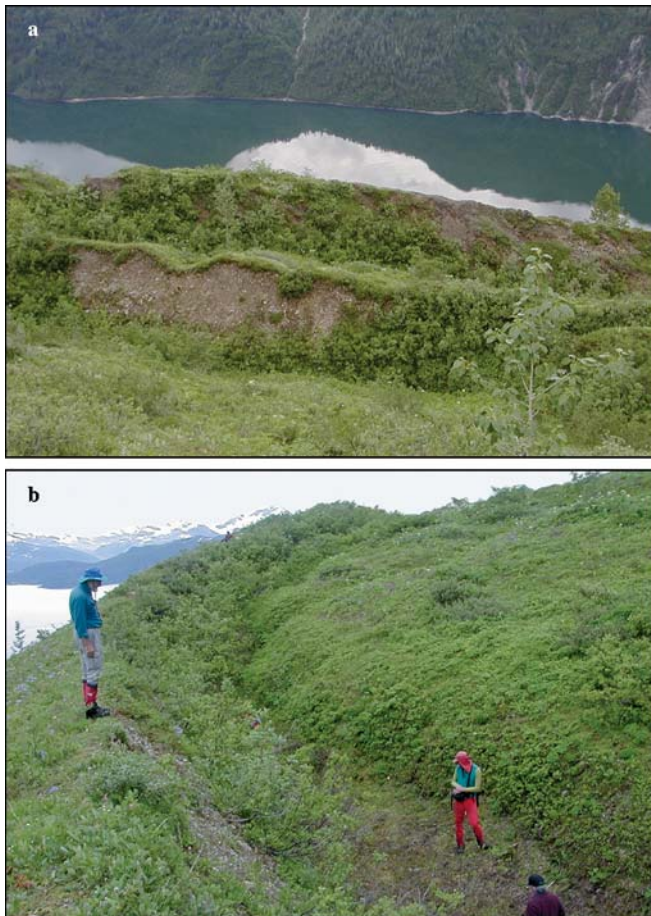


**Fig. 6** **a** Uphill-facing rotational escarpments and resulting trough, roughly perpendicular to the downslope direction. **b** Relief at one of the escarpments. Direction of landslide movement is to the left (south)

Detailed lithology, *Qs*, structure, and discontinuities in the region of the Tidal Inlet landslide were carried out during a field examination in June 2002. Based on the many separate rotational movements within the body of the landslide and the bedrock materials along the sliding surface underlying the till, the landslide is classified as a rock slump (Varnes 1978). The recent landslide features show clearly on an aerial photograph (Fig. 4). Evidence of recent movement on the Tidal Inlet landslide includes fresh scarps, back-rotated blocks, and smaller secondary landslide movements. The main scarp has a fairly uniform range of height, 20–40 m, suggesting that the body of the landslide detached rigidly. No signs of recent major renewed movement, such as slickensides, appear at any location along the base of the main scarp. The crown of the main scarp is arcuate but irregular along its length, with the highest part of the crown at an elevation of about 700 m (Fig. 4). The main scarp has a slope of 45° and exposes thinly layered bedrock of the *DSp* (Fig. 4a,b). Although small amounts of snow were observed on the slopes above the main scarp in mid-July 2002, no springs were identified along the length of the main scarp suggesting that the ground water level was generally deeper than the base of the main scarp.

The average slope angle of the existing landslide mass between the base of the main scarp and the toe of the landslide, where the rupture surface is exposed in a bedrock escarpment, is about 17°. Because of rotation of the rock slump, the original surface before sliding was steeper, approximately 32°. Likewise, should this landslide mass be more vigorously reactivated than at present, the movement of material beyond the toe would rapidly descend because of the steeper slope below the bedrock escarpment. Based on a portion of the 1:63,360 scale of the USGS Mt. Fairweather (D-2) topographic map (Fig. 3a), slope steepness from the approximate landslide center of mass to the edge of Tidal Inlet ranges from 35° to 40°.

Within the main body of the slump, the surface topography is severely disrupted by as many as 13 rotational blocks with prominent uphill-facing scarps (Figs. 4b and 6a,b). In the upper portion of the main body, the exposed portions of these blocks are within till, but further downslope, bedrock can be seen within the blocks. The back-rotated faces of these blocks are quite steep, ranging several meters in height with slope angles of 35–50°. These north-facing backscarps are thinly vegetated in places suggesting relatively recent movement. Several drainage channels through the till were found to be truncated at the crest of the rotational blocks, with the continuing channels displaced further downslope. Such disrupted drainage features indicate sudden rather than slow rotation, which would have allowed progressive incision through the erodible till blanket. Fluvial erosion could not keep pace with the up-thrusting of the blocks. The troughs formed by these blocks tend to collect snow and, because of the lack of downslope runoff, result in increased infiltration of water into the main body of the landslide. Consequently, the degree of saturation and groundwater level(s) within the landslide mass remains higher than on adjacent slopes, which reduces the relative stability of the landslide mass. Below the escarpment at the toe of the landslide, two springs were observed in July 2002 flowing from the base of the landslide talus with an estimated rate of about 10 l/s each. These springs had formed calcareous deposits on talus debris indicating that some groundwater flow was probably issuing from the limestone of the Pyramid Peak Formation above the main scarp of the landslide, although abundant calcium carbonate is also present in the *Stg*.

The toe of the landslide is exposed as layers of bedrock where the rupture surface daylight at midslope between the shoreline and the main scarp. Within the region of the toe, a 1-meter-thick

white layer of probable limestone is visible extending across the width of the landslide (Fig. 2a). This bedrock layer bulges slightly downward near the center of the toe, perhaps indicating slightly greater displacement at the center of the landslide mass. No recent displacement is evident below this bedrock exposure where till has eroded gullies extending to the shoreline.

In the center of the main body of the landslide, there is evidence of secondary landslide movement that has removed surficial material from some of the rotational blocks on the lower section of the landslide (Fig. 4b). This secondary landslide movement appears to be relatively shallow and involves mostly the till. The secondary movement appears on the 1919 Mertie photography, which does not allow determining the timing of the secondary movement in relation to the initial movement of the main body of the landslide. Cracks and fissures coincident with this secondary movement, with a maximum lateral displacement on the order of 1 m, extend up through portions of the rotational blocks within the main body of the landslide.

On the west flank of the landslide, several sets of parallel open fissures were found in surficial soils extending beyond the termination of the west side of the main scarp (below left end of yellow solid line on Fig. 4a), downslope towards the toe of the landslide. These fissures appeared relatively fresh within generally weak soils and would not be expected to be preserved for long periods of time under existing climatic conditions. In addition, revegetation would be expected to cover these fissures unless movements were recurrent. It is unclear whether these fissures represent lateral shear or collapse of surficial materials into piping voids.

### Landslide hazards

To determine the hazard from the Tidal Inlet landslide, potential velocity, current movement rates, and wave characteristics are estimated. According to Slingerland and Voight (1979), landslide velocity can be modeled from characteristics of the Tidal Inlet landslide (Table 1) as:

$$v_s = v_o + [2gs(\sin \beta - \tan \varphi_s \cos \beta)]^{1/2} \quad (1)$$

where:

- $v_s$  Landslide velocity computed as a mass sliding on a plane
- $v_o$  Initial landslide velocity (assumed to be 0 m/s)
- $g$  Gravitational constant (9.81 m/s<sup>2</sup>)

- $s$  Landslide travel distance (450 m) from toe of landslide mass to the water's edge
- $\beta$  Slope angle in degrees (40°)
- $\varphi_s$  Angle of dynamic sliding friction including pore pressure and roughness effects

The value of  $\tan \varphi_s$  is assumed to be  $0.25 \pm 0.15$  based on Slingerland and Voight (1979).

According to this formula, the impact velocity at the water is 63 m/s or 230 km/h, which was used to estimate the properties of the generated waves.

### Results of GPS measurements

Topographic monuments were installed on the Tidal Inlet landslide to assess movement rates. These points were surveyed with a dual wavelength GPS system. In 2002, 2003, and 2004, GPS data were collected for durations of at least 1 h and collection intervals of 30 s at each monument. A base station was set up over a permanent benchmark (CINCO) 7.5-km distance along the shore of the west arm of Glacier Bay and was operated simultaneously during data acquisition on the landslide monuments. All the data were processed using Trimble's TGO software, and the results provided measurements of landslide movement.

A total of four monuments were originally installed in July 2002. However, three of the four monuments were sabotaged, and only one survey monument (TI-4B), which was the lowest in elevation (526 m) located on a back-rotated slump block, remained intact for a GPS measurement in August 2003 (Fig. 4b). The results of the GPS analysis conducted during August 2003 showed that this monument moved 3.1 cm horizontally to the south (down slope) from July 2002 to August 2003.

Subsequent measurement of this monument indicated a net horizontal movement of 7.9 cm (with assessed  $2\sigma$  uncertainty of  $\pm 1.5$  cm) in a down-slope southerly direction between July 2002 and August 2004. There was no detectable vertical motion within the limits of uncertainty (last column in Table 2). Two other monuments that were reinstalled in 2003 showed movement of similar annual magnitude and direction between 2003 and 2004, providing strong evidence for consistent, very slow creeping movement of the landslide body. The continuing movement of the landslide suggests that the shear resistance may decline over time because of the weakening of geologic material resistance. The total annual movements of individual benchmarks are shown in Table 2.

**Table 1** Recently active upper portion of Tidal Inlet landslide (Fig. 4a) with characteristics and values used in calculations

Characteristic	Value
Elevation of top of scarp	700 m
Elevation of base of scarp	600 m
Landslide length (base of scarp to toe)	500 m
Landslide width (average)	700 m
Landslide width (maximum)	1,200 m
Landslide thickness (average)	30 m
Landslide travel distance to shore of Tidal Inlet	450 m
Landslide density	2.6 g/cm <sup>3</sup>
Maximum slope angle of landslide to Tidal Inlet	40°
Average slope angle of opposite shore	60°
Landslide area	293,000 m <sup>2</sup>
Landslide volume (max) block shape	10,700,000 m <sup>3</sup>
Landslide volume (min) ellipsoidal shape	5,000,000 m <sup>3</sup>
Maximum water depth (Tidal Inlet)	200 m

**Table 2** Total movement of individual bench marks and  $2\sigma$  uncertainty

Point	Interval	Horizontal (cm)	Azimuth (degrees)	Vertical (cm)	Horizontal uncertainty (cm)	Vertical uncertainty (cm)
TI-4B	2002–2003	3.1	180	−1.8	1.5	3.5
TI-4B	2003–2004	4.8	174	1.2	0.9	2.9
TI-4B	2002–2004	7.9	176	−0.6	1.5	3.6
TI-3A	2003–2004	2.0	217	−0.9	1.5	3.6
TI-5C	2003–2004	2.7	183	−1.2	1.5	3.5

All three benchmarks (Fig. 4b) have moved, although motions for TI-3A and TI-5C are just above detection based on the uncertainty limits. Motion is primarily horizontal and in a southerly direction. Vertical movement falls within the measurement uncertainty for all three movement markers and can therefore not be used to interpret landslide movement. The horizontal motion of TI-4B has the best resolution and averages  $3.8 \pm 0.7$  cm/year.

### Tsunami hazard assessment

The landslide perched on the northern shore of Tidal Inlet has the potential to generate large waves in Tidal Inlet and the western arm of Glacier Bay if it were to fail catastrophically. Landslide-generated waves are a particular concern for cruise ships transiting through Glacier Bay daily during the summer months. This section discusses the range of wave amplitudes and periods in the western arm of Glacier Bay resulting from a catastrophic landslide in Tidal Inlet.

Modeling waves generated by sudden failure of landslide blocks entering fjords present several difficulties. First, an appropriate wave generation model linked to the geometric and kinematic parameters of the landslide must be implemented. The landslide and water impact involves turbulent and nonlinear flow that can only be approximated by modeling. In addition, catastrophic slope failure into fjords can result in a wave run-up on the opposite shore, as was observed after the 1958 Lituya Bay landslide (Fritz et al. 2001; Mader and Gittings 2002). Run-up and backwash is strongly nonlinear and involves a complex parameterization of overland flow. Finally, resonance of wave action in fjords can also be nonlinear, depending on the aspect ratio of the fjord and the amplification at resonance (see Appendix). Walder et al. (2003) made an important distinction between subaerial landslides that impact the water at an initial velocity and come to rest during a relatively short submergence time (termed initial-velocity cases) and those subaerial landslides that start near the water edge and move for a relative long submergence time down a steep subaqueous slope (termed release-from-shore cases). For perched landslides entering flat-bottom fjords, such as the Tidal Inlet landslide scenario, the hydrodynamics are best represented by the initial-velocity case.

Near-field estimates are made of the amplitude of the leading wave from a scaling relationship. Then, using a landslide-impact wave generation model to specify initial conditions, propagation of waves within Tidal Inlet and into the western arm of Glacier Bay is numerically computed using available bathymetric data. A more detailed description of the analysis is given by Geist et al. (2003).

### Near-field wave estimates

It is convenient to separate different stages of wave evolution emanating from subaerial landslides as indicated by Walder et al. (2003): splash zone (near the site of impact), near field, and far field. The hydrodynamics of the splash zone involves a high degree of complexity that is only recently being understood through physical and numerical models (Fritz et al. 2001; Mader and Gittings 2002; Liu et al. 2005; Fritz 2006; Lynett and Liu 2006).

Because the primary objective of this study is to estimate the range of tsunami wave heights outside of Tidal Inlet, scaling relationships can be used to determine the height of the leading elevation wave generated from a subaerial landslide just outside the splash zone. For this purpose, the measured parameters and the underlying assumptions of the method proposed by Huber and Hager (1997) are used. For the maximum volume ( $>10$  Mm<sup>3</sup>) landslide into Tidal Inlet, the wave height in the center of the inlet is estimated to be 77 m. This estimate is used to constrain the impact generation model that specifies the initial conditions for far-field propagation in the next section.

### Numerical model of hydrodynamics

To calculate the wave motion in Glacier Bay using realistic bathymetry, wave propagation generated by an initial-velocity landslide into Tidal Inlet is modeled using a numerical method. The initial tsunami wave field is determined from a landslide-impact model parameterized using the velocity, density, and effective dimension of the landslide. Wave propagation is then modeled using the shallow-water wave equations, where the wavelength is considered to be significantly greater than the water depth.

The initial velocity of the Tidal Inlet landslide entering the water is estimated to be 63 m/s (previously calculated in “Landslide hazards”). This velocity is greater than the phase speed of long waves (or celerity) in the inlet, resulting in an impact Froude number ( $Fr = v_{slide} / \sqrt{gh}$ , where  $h$  is water depth) of approximately 1.4. For comparison, the estimated velocity of the 1958 Lituya Bay slide is 110 m/s with an impact Froude number of 3.18 (Fritz et al. 2001). For Tidal Inlet, the 77-m leading wave amplitude estimated from scaling relationships results in an amplitude/water depth ratio of approximately 0.4, which is within the range of values measured in flume experiments for  $Fr \sin\theta = 0.9$ – $1.3$  (where  $\theta$  is the near shore slope) by Walder et al. (2003).

Previous generation models for initial-velocity and release-from-shore slides (e.g., Walder et al. 2003; Liu et al. 2005) were developed for slopes that are significantly less steep than what is present on the northern shore of Tidal Inlet ( $35$ – $40^\circ$ ). For these steep slopes, it is assumed that the slide will behave more as a free-fall-impacting object, rather than as a wave maker source. Therefore, the impact model of Ward and Asphaug (2000, 2002) was developed for asteroid-generated tsunamis to define the initial conditions for wave propagation. This model is chosen because of the direct connection between impact kinematics and wave field away from the source. In addition, this model is consistent with waves calculated using fully three-dimensional simulations of impacts (Ward and Asphaug 2000). The initial wave field from an impact is a parabolic cavity of maximum depth  $D_C$  and inner and outer radii  $R_C$  and  $R_D$ , respectively:

$$\eta(r) = D_C \left[ 1 - \left( \frac{r}{R_C} \right)^2 \right] \quad r \leq R_D$$

$$\eta(r) = 0 \quad r > R_D \quad (2)$$

As indicated by Ward and Asphaug (2000, 2002), if  $R_D = \sqrt{2}R_C$ , then the volume of water displaced from the cavity is preserved along the outer edge as a leading elevation wave. The Schmidt and Holsapple (1982) scaling relationship links the impactor kinematics (velocity,  $V_i$ ; radius,  $R_i$ ; and density,  $\rho_i$ ) to the cavity radius ( $R_C$ ):

$$R_C = R_i \left[ \left( \frac{1}{3.22} \right) \frac{V_i^2}{gR_i} \right]^\beta \left( \frac{\rho_i}{\rho_t} \right)^{1/3} \left( \frac{C_t}{1.24} \right), \quad (3)$$

where  $\beta$  and  $C_t$  are target properties ( $\beta=0.22$  and  $C_t=1.88$ , see Ward and Asphaug 2000) and  $\rho_t$  is the target density (in this case water,  $\rho_t=1.0 \text{ g/cm}^3$ ). Cavity depth ( $D_C$ ) is related to the cavity radius by the following expression:

$$D_C = qR_C^\alpha, \quad (4)$$

where  $\alpha = 1/(2\beta) - 1$  and  $q$  can be determined as described from Schmidt and Holsapple (1982). Ward and Asphaug (2000) indicated that the effect of these parameters is that deeper and narrower cavities are created by smaller diameter impactors traveling at the same velocity.

Because the dimensions of the potential Tidal Inlet landslide are not radially symmetric and it is unknown as to how the shape of the slide will change during failure and disintegration, an effective impact radius is calculated from the height of the landslide-generated wave using the method of Huber and Hager (1997). Using an impact velocity of 67 m/s and an associated wave height of 77 m, the effective impact radius is 115 m. Fritz et al. (2001) noted that the wave height for the Lituya Bay landslide is underestimated using the method of Huber and Hager (1997), primarily because landslides used to develop this relation were thinner than the Lituya Bay landslide (thickness=92 m, compared to an estimated 30 m for the potential Tidal Inlet landslide). It is therefore possible that the Huber and Hager (1997) method is more applicable for estimating wave heights in Tidal Inlet than for Lituya Bay.

To account for the nonequidimensional impactor shape of a subaerial landslide like the potential Tidal Inlet landslide, we modify the impact shape function from the canonical parabolic cavity to an elliptic paraboloid of the form:

$$\eta(x, y) = D_C \left[ 1 - \left( \frac{x}{R_{Cx}} \right)^2 - \left( \frac{y}{R_{Cy}} \right)^2 \right], \left( \frac{x}{R_{Cx}} \right)^2 + \left( \frac{y}{R_{Cy}} \right)^2 \leq 2 \quad (5)$$

$$\eta(x, y) = 0, \left( \frac{x}{R_{Cx}} \right)^2 + \left( \frac{y}{R_{Cy}} \right)^2 > 2$$

The same cavity depth is used as for the parabolic cavity, and the cavity radius in the direction of the landslide motion ( $R_{Cy}$ ) is set equal to the parabolic cavity radius above. The cavity radius perpendicular to the landslide motion ( $R_{Cx}$ ) is varied to accommodate different landslide widths.

With the initial wave field specified from the modified landslide-impact source model (Eq. 5), wave propagation is calculated using a numerical approximation to the shallow water wave equations (e.g., Aida 1969; Geist 2002; Satake 2002). This method used a standard finite-difference algorithm on a staggered grid ( $\Delta x$ ) in which the time step for the calculations ( $\Delta t$ ) is constrained by the Courant-Friedrichs-Lewy stability criterion:  $\Delta t \leq \Delta x / \sqrt{2gh}$ . The bathymetry used in the calculations is derived from recently acquired multibeam data (Carlson et al. 2003) merged with older National Oceanic and Atmospheric Administration data and

gridded at a 60-m spacing. The time step used in all simulations is 0.5 s, and the total duration is up to 3 h. At open boundaries, a radiation boundary condition is used (Reid and Bodine 1968). At land-ocean boundaries, a total reflection boundary condition is used. For regions where there is significant wave run-up (e.g., broadside from the source region), the reflection boundary condition may overestimate amplitudes of reflected waves that, with overland flow, would be dissipated by frictional forces. In addition to reflected and refracted waves propagating throughout the waterways, there also are coastal-trapped waves that are strongest with gentle near-shore slopes (Liu et al. 2005; Lynett and Liu 2006). These waves can be approximately modeled with the method applied in this study.

## Results

The wave history at any particular location in the study region can be characterized by the (a) first arrival of waves emanating from the source followed by (b) a complex wave train or coda resulting from reflections, scattering, and trapped waves. Outside Tidal Inlet, the first arrivals may include a direct phase, depending on the ray path to the target location, followed by simple reflection phases. The first waves have a longer period than waves in the coda and can be thought of as cylindrical waves emanating from the mouth of Tidal Inlet as described in the resonance analysis (Appendix). Figure 7 shows eight snapshots of model wave propagation from shortly after generation through the first hour.

The waves reverberate within Tidal Inlet and eventually pass through the mouth and into the western arm of Glacier Bay as a series of cylindrical waves. As the waves pass from shallow water (point o) into the deeper waters of Glacier Bay (point 1), the wavelength increases, and the amplitude decreases according to Green's Law:

$$\frac{\eta_1}{\eta_0} = \left( \frac{b_0}{b_1} \right)^{1/2} \left( \frac{h_0}{h_1} \right)^{1/4} \quad (6)$$

where  $b_1/b_0$  represents the spreading of ray paths ( $b$  is the distance between rays) and  $h_1/h_0$  represents the fractional change in depth (Satake 2002). As the waves re-enter shallow water, the amplitude increases, and the wavelength decreases. This is especially evident for the later times (Fig. 7;  $t=30, 60$  min) where the shallow reaches of the waterways have higher amplitude and shorter-period waves.

These characteristics can also be demonstrated by examining synthetic wave time history records or marigrams for several points in the model domain. Six hypothetical wave gauges are positioned from the mouth of Tidal Inlet, across the western arm of Glacier Bay, and in Blue Mouse Cove (Fig. 7;  $t=0$  min). Figure 8a shows marigrams for the first 10 min after the landslide enters Tidal Inlet.

A reduction in wave amplitude in the central part of Glacier Bay is evident on Fig. 8 (stations 4 and 5), with a slight increase in first-arrival amplitude in Blue Mouse Cove (station 6). Also evident in the marigrams for stations 1 and 2 is the longer-period response of the first arrival compared to the broadband coda that follows. The hydrodynamic simulation is recomputed for an average slide width of 700 m. The synthetic marigrams are shown in Fig. 8b. Most noticeable is an increase in short-period

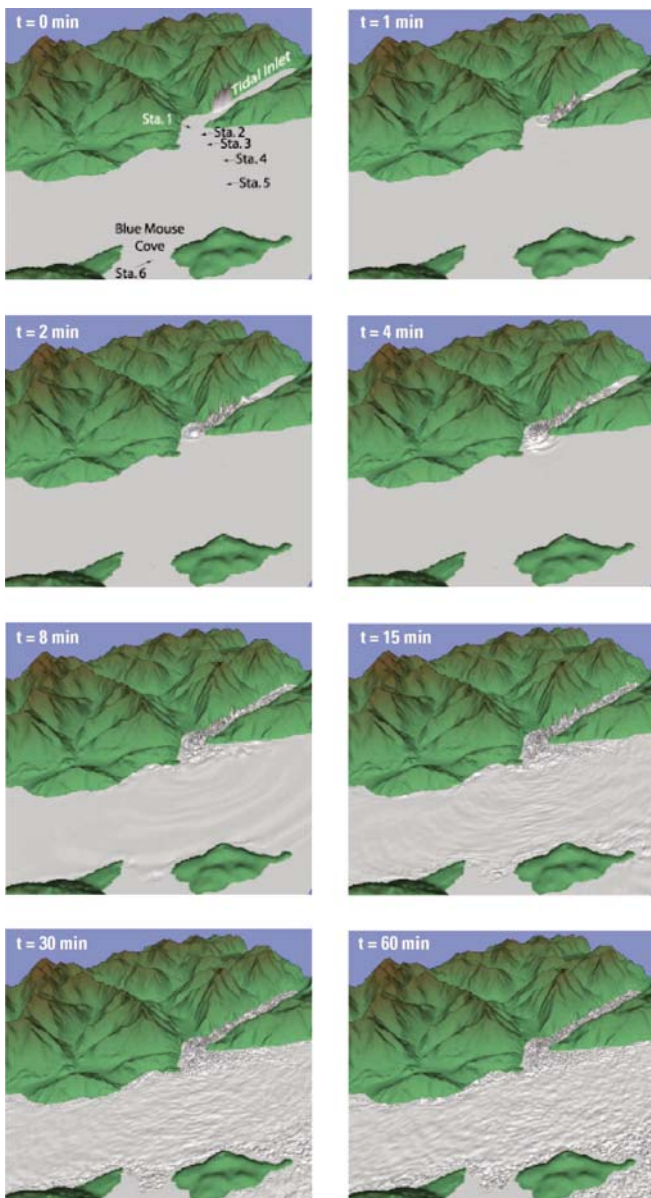


**Fig. 7** Eight snapshots of the tsunami propagation simulation. View to the northeast. Snapshot at  $t=0$  min shows synthetic wave gauge station locations

waves in the first arrivals and coda for the smaller slide. In addition, the maximum wave amplitude appears to be slightly less for the smaller slide.

The decay of wave action in Glacier Bay from a landslide-generated wave source in Tidal Inlet is difficult to determine, owing to complex reflections from the adjoining shorelines and resonance within Tidal Inlet. Optimally, a remote observation system would be available with which to assess the wave activity in Glacier Bay after a major subaerial slide occurs. This could include land-based or airborne visual observations and/or telemetered wave-gauge recordings.

### Discussion

Numerical simulations of waves generated by a major subaerial landslide in Tidal Inlet indicate that significant wave activity

would occur in the western arm of Glacier Bay for more than several hours. A landslide-impact source model, consistent with the findings of Fritz et al. (2001) and Mader and Gittings (2002) for waves generated by the 1958 Lituya Bay slide, is used to specify the initial conditions for wave propagation in the Glacier Bay waterways. The kinematic and geometric parameters for the slide are taken from field examination. Analytic studies of resonance in a narrow and elongated bay indicate that the first several modes of resonance are excited by much longer wave periods than are likely to be generated by a Tidal Inlet subaerial landslide. Wave trains of long duration are caused by oscillations at the source that are characteristic of impact-type-generating mechanisms (Momoi 1964; Ward and Asphaug 2000). Also contributing to the long duration is cross-channel-resonance and the site-specific response at locations outside Tidal Inlet.

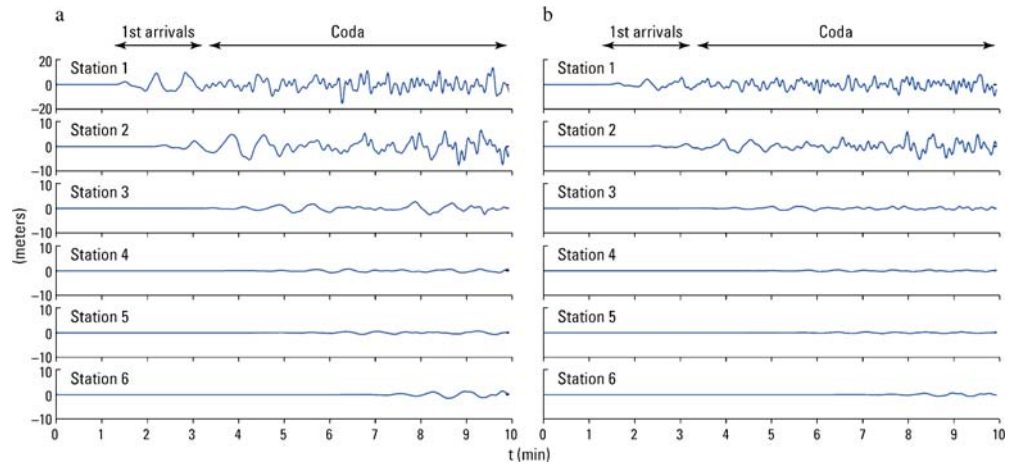
The maximum volume slide generates very high waves (tens of meters in amplitude with possible greater-than-100-m wave run-up) near the source in Tidal Inlet. It is likely that very-high-amplitude waves would persist throughout Tidal Inlet. Outside the inlet, waves of significant amplitude ( $>10$  m) occur in shallow water regions, especially near the mouth of Tidal Inlet. In the deep waterways of the western arm of Glacier Bay, the wave amplitude decreases with distance according to Green's Law. A landslide with less volume would generate waves with shorter periods throughout the first arrivals and coda of the wave train. Differences in waveforms at different locations in Glacier Bay are primarily dependent on the local bathymetry, whereas changes in slide parameters primarily influence the overall amplitude of waves. Because the total duration of slide-generated waves is difficult to accurately predict, it is recommended that a remote observation system (e.g., wave gauge) be installed to assess when significant wave activity after a major subaerial landslide has subsided.

The impact to cruise ships and other vessels in the region to these waves likely depends on which part of the wave train the ships encounter as well as the direction of wave impact against the longitudinal axis of the ships. Near the mouth of Tidal Inlet, the amplitude of waves is greatest within approximately 40 min after the landslide enters the water. Moreover, the first arrivals here and elsewhere in the vicinity of Tidal Inlet are likely to be long-period waves (periods of up to 1 min) and approximately unidirectional: that is, can be characterized as cylindrical waves emanating from the mouth of Tidal Inlet. In contrast, the coda of the wave train is caused by multiple reflected, scattered, and trapped waves that are broadband and have a wide range of incidence angles.

### Conclusions

Initial GPS results indicate that the Tidal Inlet landslide is moving very slowly to the south down slope at a rate of  $\sim 3\text{--}4$  cm/year. The magnitude of movement is well above the conservative estimate of uncertainty. Continued monitoring will help to characterize the nature of movement over a longer time frame. Investigation indicates that a catastrophic, rapid failure of the landslide would result in a significant hazard to park visitors in the vicinity of Tidal Inlet. Depending on the timing and impact direction, there is a considerable chance of ship damage or foundering with associated potential loss of life. This study alone has shown that continued monitoring may be crucial to avoid a potential future tragedy.

**Fig. 8** Synthetic marigrams wave height for six station locations shown in Fig. 8 ( $t=0$  min) for a duration of 10 min. Note that the vertical scale for Station 1 (top) is  $\pm 20$  m, whereas for the other stations, the scale is  $\pm 10$  m. **a** Wave calculations for the maximum slide width (1,200 m); **b** wave calculation for the average slide width (700 m)



### Acknowledgments

Sandra Zirnheld of the Geophysical Institute, University of Alaska, and Patricia Craw (Patricia Burns) of the Alaska Division of Geological and Geophysical Surveys assisted us with the initial field examination of the landslide in Tidal Inlet. Ernst Jakob volunteered his time and assisted with the fieldwork. Ellie Boyce and Chris Larsen of the Geophysical Institute, University of Alaska, Fairbanks, Alaska, worked on the GPS measurements of the landslide with Roman Motyka. Peter Dartnell, USGS, helped merge various bathymetric data sets for the hydrodynamic modeling. David Jones, USGS, prepared and improved the figures in the text. Homa Lee and Jeff Coe, USGS, are acknowledged for their review of the initial version of the paper. More recent review of the paper was improved by a journal reviewer, Doug VanDine and editor, Prof. Uldrich Hungr.

### Appendix

#### Resonance of Tidal Inlet: Analytic Approach

The geometry of Tidal Inlet is ideally suited to allow a determination of the modes of natural resonance using analytic expressions. For example, Rogers and Mei (1978) used a rectangular bay geometry with a width  $2a$  and length  $L$  (Fig. 9).

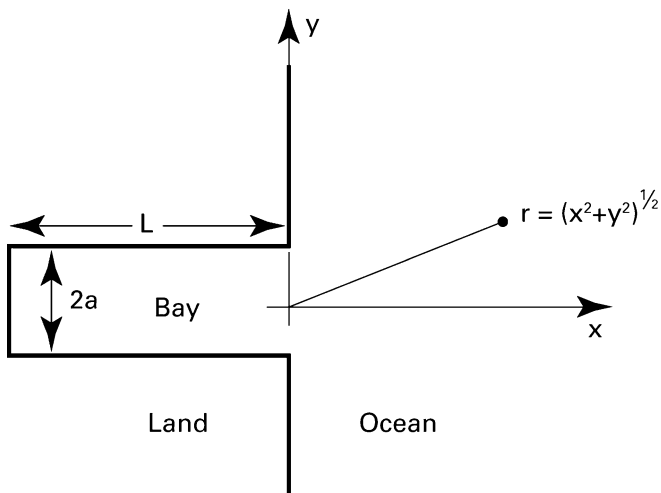


**Fig. 9** Geometry and coordinate system for a narrow bay

The resonant modes are determined using the Boussinesq equations at a constant water depth ( $h$ ) that include the effects on nonlinearity and dispersion:

$$\begin{aligned} \eta_t + \nabla u + \nabla(\eta u) &= 0 \\ u_t + \nabla \eta + \frac{1}{2} \nabla u^2 + \frac{1}{3} \mu^2 \nabla \eta_{tt} &= 0 \end{aligned} \quad (7)$$

where  $\eta$  is the water surface displacement,  $u$  is the depth-averaged horizontal velocity field, and the small parameter  $\mu$  is defined by  $\mu^2 = \omega^2 h / g$  where  $\omega$  is frequency and  $h$  is water depth. The variables in Eq. 7 have been nondimensionalized with respect to characteristic length and time scales.

The resonant wave numbers ( $k_r$ ) are given by

$$(k_r l) \cong \left(m + \frac{1}{2}\right) \pi + \left[ \left(\frac{1}{k_r l}\right) \text{Im} Z \right]_{k_r l = (m + \frac{1}{2}) \pi} \quad m = 0, 1, 2, \dots, K \quad (8)$$

where  $l$  is the nondimensional length of the bay. The entrance impedance of the bay ( $Z$ ) is defined by Rogers and Mei (1978) as

$$Z = k^2 \delta \left[ 1 + \frac{2i}{\pi} \ln \left( k \delta \frac{2\gamma}{\pi e} \right) \right] \quad (9)$$

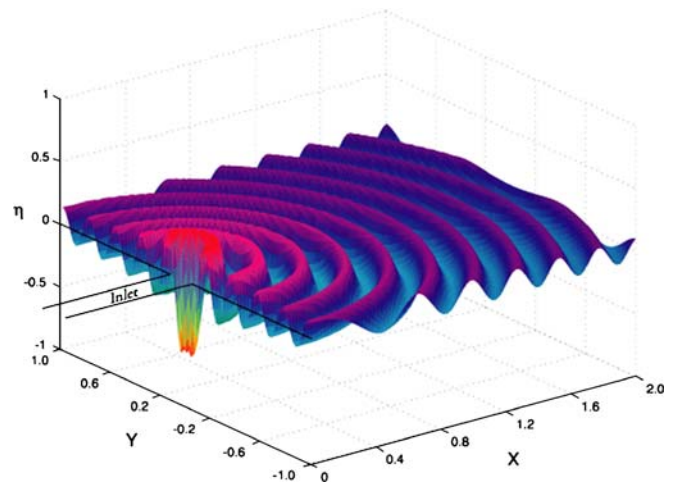


**Fig. 10** Modeled radiant component of wave field in Glacier Bay outside the Tidal Inlet from resonance involving monochromatic input. Axes in nondimensional units

where  $2\delta$  is the nondimensional bay width and  $\gamma$  is Euler's constant. The aspect ratio of Tidal Inlet is approximately  $\frac{2\delta}{T} = \frac{1}{7}$  such that the first two resonant modes are  $(k_r L)_1 = 1.272$  and  $(k_r L)_2 = 4.050$ . These modes are slightly less than the  $1/4$  and  $3/4$  wavelength resonant modes predicted by a simple "quarter-wavelength resonator" (Raichlen and Lee 1992). At resonant antinodes, there is no additional amplification of waves from resonance within the bay (i.e., unit response).

Outside the bay and far from the entrance, nonlinear effects can be ignored. Rogers and Mei (1978) indicated that most bay and harbor resonant problems can be decoupled so that the nonlinear theory is used within the bay and the linear theory is used in the ocean. The radiated wave from the bay, exclusive of incident and reflected waves outside the bay, is given by the following expression (Rogers and Mei 1978):

$$\eta_{\text{rad}} = iTk\delta \sin(kl)H_0^{(1)}(kr) \quad (10)$$

where  $r^2 = x^2 + y^2 \gg \delta$ ,  $x > 0$  (Fig. 9),  $H_0^{(1)}(kr)$  is the Bessel function of the third kind (Hankel function), and

$$T = A[\cos(kl) - (iZ/k) \sin(kl)]^{-1} \quad (11)$$

where  $A$  is the nondimensional amplitude of the incident wave. The wave field from Eq. 11 is shown in Fig. 10.

When considering the effects of resonance on transient waves, Kowalik (2001) also noted that resonant amplification also depends on the duration of the wave train. Short wave trains, relative to bay length, will not last long enough to set up resonance. Resonance in elongated coastal inlets may be more of a concern with longer-period waves from large seismogenic tsunamis (Carrier and Shaw 1970; Henry and Murty 1995).

## References

- Aida I (1969) Numerical experiments for the tsunami propagation—the 1964 Niigata tsunami and the 1968 Tokachi-Oki tsunami. *Bull Earthq Res Inst Univ Tokyo* 47: 673–700
- Brew DA, Horner RB, Barnes DF (1995) Bedrock-geologic and geophysical research in Glacier Bay National Park and Preserve: unique opportunities of local to global significance. In: Engstrom DR (ed) *Proceedings of the Third Glacier Bay Science Symposium*, 1993. National Park Service, Anchorage, Alaska, pp 5–14
- Carlson PR, Hooge PN, Cochrane GR, Stevenson AJ, Dartnell P, Stone JC (2003) Multibeam bathymetry and selected perspective views of Glacier Bay, Alaska. *USGS Water Resources Investigations Report* 03-4141
- Carrier GF, Shaw RP (1970) Response of narrow-mouthed harbors. In: Adams WM (ed) *Tsunamis in the Pacific Ocean*. East-West Center, Honolulu, pp 377–398
- Fritz HM (2006) Physical modeling of landslide generated tsunami. In: Mercado A, Liu PLF (eds) *Caribbean tsunami hazard*. World Scientific, Singapore, pp 308–324
- Fritz HM, Hager WH, Minor HE (2001) Lituya Bay case: rockslide impact and wave run-up. *Sci Tsunami Hazards* 19:3–22
- Geist EL (2002) Complex earthquake rupture and local tsunamis. *J Geophys Res* 107:E5E 2-1–E5E 2-15
- Geist EL, Jakob M, Wiczorek GF, Dartnell P (2003) Preliminary hydrodynamic analysis of landslide-generated waves in Tidal Inlet, Glacier Bay National Park, Alaska. *US Geological Survey, Open-File Report* 03-411
- Goodwin RG (1988) Holocene glaciolacustrine sedimentation in Muir Inlet and ice advance in Glacier Bay, Alaska, U.S.A. *Arct Alp Res* 20:55–69
- Henry RF, Murty TS (1995) Tsunami amplification due to resonance in Alberni Inlet. In: Tsuchiya Y, Shuto N (eds) *Tsunami: progress in prediction, disaster prevention and warning: advances in natural and technological hazards research*. Kluwer, Dordrecht, The Netherlands, pp 117–128
- Hooge PN, Hooge ER, Dick CA, Solomon EK (2000) Glacier Bay oceanography and the oceanographic analyst GIS extension: CD-ROM set. *US Geological Survey, Alaska*
- Huber A, Hager WH (1997) Forecasting impulse waves in reservoirs. In: *Dix-neuvième Congrès des Grands Barrages*, Florence, Commission Internationale des Grands Barrages, pp 993–1005
- Kowalik Z (2001) Basic relations between tsunamis calculation and their physics. *Sci Tsunami Hazards* 19:99–116
- Larsen CF, Motyka RJ, Freymueller JT, Echelmeyer KA, Ivins ER (2005) Rapid viscoelastic uplift in southeast Alaska caused by post-Little Ice Age glacial retreat. *Earth Planet Sci Lett* 237:548–560
- Liu PLF, Wu TR, Raichlen F, Synolakis CE, Borrero JC (2005) Runup and rundown generated by three-dimensional sliding masses. *J Fluid Mech* 536:107–144
- Lynett P, Liu PLF (2006) Three-dimensional runup due to submerged and subaerial landslides. In: Mercado A, Liu PLF (eds) *Caribbean tsunami hazard*. World Scientific, Singapore, pp 289–307
- Mader CL, Gittings ML (2002) Modeling the 1958 Lituya Bay mega-tsunami. II. *Sci Tsunami Hazards* 20:241–250
- Mann DH (1986) Wisconsin and Holocene glaciation of southeast Alaska. In: Hamilton TD, Reed KM, Thorson RM (eds) *Glaciation in Alaska—the geologic record*. Alaska Geological Society, Anchorage, pp 237–262
- Miller DJ (1954) Cataclysmic flood waves in Lituya Bay, Alaska. *Geol Soc Amer Bull* 65:1346
- Miller DJ (1960) Giant waves in Lituya Bay, Alaska. *US Geol Surv Prof Pap* 354C:51–83
- Miller RD (1975) Surficial geologic map of the Juneau urban area and vicinity, Alaska. *US Geological Survey Miscellaneous Investigations Series Map* I-885, 1:48,000
- Molenaar D (1990) Glacier Bay and Juneau Icefield region and the glacierized ranges of Alaska–Northwestern Canada: pictorial Landform Map. *Molenaar Landform Maps*, Burley, WA
- Momoi T (1964) Tsunami in the vicinity of a wave origin [I]. *Bull Earthq Res Inst Univ Tokyo* 42:133–146
- Motyka RJ, Beget JE (1996) Taku Glacier, southeast Alaska, U.S.A.: Late Holocene history of a tidewater glacier. *Arct Alp Res* 28(1):42–51
- Motyka RJ, O'Neil S, Connor C, Echelmeyer KA (2002) 20th Century thinning of Mendenhall Glacier, Alaska, and its relationship to climate, lake calving, and glacier run-off. *Glob Planet Change* 35(1–2):93–112
- Müller L (1964) The rock slide in the Vajont Valley. *Felsmech Ingenieurgeol* 11/3–4: 148–212
- Müller L (1968) New considerations on the Vaiont slide. *Felsmech Ingenieurgeol* VI/4: 1–91
- Plafker G, Thatcher W (1982) Geological and geophysical evaluation of the mechanisms of the great 1899–1900 Yakutat Bay, Alaska, earthquakes. Program and Abstracts, AGU Conference on fault behavior and the earthquake generating process, Snowbird, UT, Oct. 11–15, 1982 (abstract)
- Post A, Motyka RJ (1995) Taku and LeConte Glaciers, Alaska. Calving speed control of late Holocene asynchronous advances and retreats. In: Nelson FE (ed) *Glaciers and late quaternary environments of Alaska: I, essays in honor of William O. Field*. *Phys Geogr* 16:59–82
- Raichlen F, Lee JJ (1992) Oscillation of bays, harbors, and lakes. In: *Herbich JB (ed) Handbook of coastal and ocean engineering*. Gulf, Houston, TX, pp 1073–1113
- Reid HF (1896) Glacier Bay and its glaciers. *US Geological Survey 16th Annual Report*, Part 1, pp 421–461
- Reid RO, Bodine BR (1968) Numerical model for storm surges in Galveston Bay. *J Waterw Harb Div* 94:33–57
- Rogers SR, Mei CC (1978) Nonlinear resonant excitation of a long and narrow bay. *J Fluid Mech* 88:161–180
- Rossmann DL (1963) Geology of the eastern part of the Mount Fairweather quadrangle—Glacier Bay, Alaska. *US Geol Surv Bull* 1121-K:K1–K57

---

Satake K (2002) Tsunamis. In: Lee WHK, Kanamori H, Jennings PC, Kisslinger C (eds) International handbook of earthquake and engineering seismology, International Association of Seismology and Physics of the Earth's Interior, Part A. Academic, London, p 932

Schmidt RM, Holsapple KA (1982) Estimates of crater size for large-body impacts: gravitational scaling results. In: Silver LT, Schultz PH (eds) Geological implications of impacts of large asteroids and comets on the Earth. Geological Society of America Special Paper 190, Boulder, CO, pp 93–102

Semenza E, Ghirrotti M (2000) History of the 1963 Vaiont slide: the importance of geological factors. Bull Eng Geol Environ 59:87–97

Slingerland RL, Voight B (1979) Occurrences, properties, and predictive models of landslide-generated water waves. In: Voight B (ed) Developments in geotechnical engineering 14B: rockslides and avalanches, 2, engineering sites. Elsevier, New York, pp 317–397

Varnes DJ (1978) Slope movement types and processes. In: Schuster RL, Krizek RJ (eds) Landslides—analysis and control: transportation research board special report 176. National Academy of Sciences, Washington, DC, pp 11–33

Walder JS, Watts P, Sorensen OE, Janssen K (2003) Tsunamis generated by subaerial mass flows. J Geophys Res 108:EPM2-1

Ward SN, Asphaug E (2000) Asteroid impact tsunami: a probabilistic hazard assessment. Icarus 145:64–78

Ward SN, Asphaug E (2002) Impact tsunami—Eltanin. Deep-Sea Res Part 2 49:1073–1079

**G. F. Wiczorek** (✉) · **E. L. Geist**

US Geological Survey,  
345 Middlefield Road,  
Menlo Park, CA 94025, USA  
e-mail: gwiczor@usgs.gov

**E. L. Geist**

e-mail: egeist@usgs.gov

**R. J. Motyka** (✉)

Geophysical Institute, University of Alaska Fairbanks,  
835 Dixon Street,  
Juneau, AK 99801, USA  
e-mail: roman.motyka@uas.alaska.edu

**M. Jakob**

BGC Engineering,  
Suite 500-1045 Howe Street,  
Vancouver, BC V6Z, 2A9, Canada  
e-mail: mjakob@bgcengineering.ca